

# BAYESIAN ANALYSIS OF SPARSE ANISOTROPIC UNIVERSE MODELS AND APPLICATION TO THE 5-YR WMAP DATA

NICOLAAS E. GROENEBOOM<sup>1</sup> AND HANS KRISTIAN ERIKSEN<sup>1,2</sup>

(Dated: September 14, 2008)  
*Draft version September 14, 2008*

## ABSTRACT

We extend the previously described CMB Gibbs sampling framework to allow for exact Bayesian analysis of anisotropic universe models, and apply this method to the 5-year WMAP temperature observations. This involves adding support for non-diagonal signal covariance matrices, and implementing a general spectral parameter MCMC sampler. As a worked example we apply these techniques to the model recently introduced by Ackerman et al., describing for instance violations of rotational invariance during the inflationary epoch. After verifying the code with simulated data, we analyze the foreground-reduced 5-year WMAP temperature sky maps. For  $\ell \leq 400$  and the W-band data, we find tentative evidence for a preferred direction pointing towards  $(l, b) = (110^\circ, 10^\circ)$  with an anisotropy amplitude of  $g_* = 0.15 \pm 0.039$ . Similar results are obtained from the V-band data [ $g_* = 0.10 \pm 0.04$ ;  $(l, b) = (130^\circ, 20^\circ)$ ]. Further, the preferred direction is stable with respect to multipole range, seen independently in both  $\ell = [2, 100]$  and  $[100, 400]$ , although at lower statistical significance. We have not yet been able to establish a fully satisfactory explanation for the observations in terms of known systematics, such as non-cosmological foregrounds, correlated noise or asymmetric beams, but stress that further study of all these issues is warranted before a cosmological interpretation can be supported.

*Subject headings:* cosmic microwave background — cosmology: observations — methods: numerical

## 1. INTRODUCTION

Since the early 1990's, great advances have been made in the field of data analysis techniques for studying the cosmic microwave background (CMB). Observations of the CMB anisotropies, for instance those made by the Wilkinson Microwave Anisotropy Probe (WMAP) experiment (Bennett et al. 2003; Hinshaw et al. 2007), provides the single most powerful probe in contemporary cosmology. From these, various theoretical universe models may be constrained, and today an effective concordance model based on the inflationary  $\Lambda$ CDM framework has been established.

The theory of inflation was initially proposed as a solution to the horizon and flatness problem (Guth et al 1981). Additionally, it established a highly successful theory for the formation of primordial density perturbations, thus providing the required seeds for the large-scale structures (LSS), later giving rise to the temperature anisotropies in the cosmic microwave background radiation that we observe today (Starobinsky 1980; Guth et al 1981; Linde et al. 1982; Mukhanov et al. 1981; Starobinsky et al 1982; Linde et al. 1983, 1994; Smoot et al. 1992; Ruhl et al 2003; Runyan et al. 2003; Scott et al. 2003).

A firm prediction of inflation is that the observed universe should be nearly isotropic on large scales. Yet, recent theoretical studies have demonstrated that anisotropic inflationary models are indeed conceivable (Armendariz-Picon 2006; Emir Gümrükçüoglu et al. 2007; Pullen & Kamionkowski 2007; Kanno et al. 2008;

Electronic address: nicolaag@astro.uio.no

Electronic address: h.k.k.eriksen@astro.uio.no

<sup>1</sup> Institute of Theoretical Astrophysics, University of Oslo, P.O. Box 1029 Blindern, N-0315 Oslo, Norway

<sup>2</sup> Centre of Mathematics for Applications, University of Oslo, P.O. Box 1053 Blindern, N-0316 Oslo, Norway

Yokoyama & Soda 2008). Two other examples are those presented by Ackerman et al. (2007) (ACW) and Erickcek et al. (2008). The first model considers violation of rotational invariance in the early universe, while the second model describes the effects on the observed perturbation distribution due to a large-scale curvaton field.

The introduction of anisotropic models poses several problems in terms of data analysis. The definition of a proper likelihood function may be non-trivial for a general case, although many models can be described as multivariate Gaussians with non-diagonal covariance matrices. All models mentioned above are examples of this. Yet, even in these relatively simple cases, the numerical evaluation of the likelihood is computationally unfeasible due to the sheer size of the relevant covariance matrix.

In the present paper, we extend the previously described CMB Gibbs sampling framework (Jewell et al. 2004; Wandelt et al. 2004; Eriksen et al. 2004b) to allow for non-diagonal, but sparse, covariance matrices. As currently described in the literature, this framework allows for exact Bayesian analysis of high-resolution CMB data, but only under the assumption of isotropy, i.e., a diagonal CMB covariance matrix. This method has already been applied several times to the WMAP data (O'Dwyer et al. 2004; Eriksen et al. 2007a,b, 2008b), and has been extended to take into account both polarization (Larson et al. 2007) and internal component separation (Eriksen et al. 2008a).

The question of isotropy has received considerable attention during recent years, due to unexpected signatures observed in the WMAP sky maps. These data appear to exhibit several significant and distinct signatures of violation of statistical isotropy. First, de Oliveira-Costa et al. (2004) found a striking alignment between the two largest harmonic modes in the temperature anisotropy sky, the

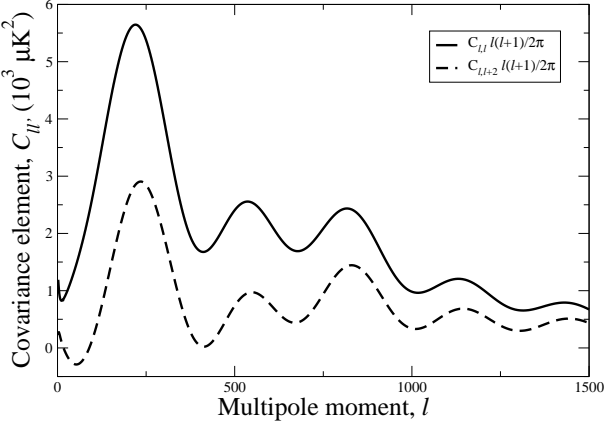


FIG. 1.— Covariance elements,  $C_{\ell,\ell}$  and  $C_{\ell,\ell+2}$ , used in the construction of the ACW covariance matrix. These are computed by modifying CAMB, a publicly available Boltzmann code.

quadrupole and the octopole. Second, Vielva et al. (2004) pointed out the presence of a very large cold spot in the southern Galactic sky, apparently incompatible with  $\Lambda$ CDM-based simulations. Finally, Eriksen et al. (2004a) found a significantly anisotropic distribution of power between two hemispheres. The tools developed in the present paper may be able to constrain specific models relevant for these observations. In particular, we use these methods to estimate the anisotropy parameters in the ACW model from the 5-year WMAP temperature data.

The paper is structured as follows: In §2, we review the ACW universe model, and briefly introduce the relevant posterior distribution. Next, we present the method in §3, before we apply our tools to simulated data in §4. In §5 we analyze the five-year WMAP temperature sky maps. Finally, we conclude in §6.

## 2. THE ANISOTROPIC ACW UNIVERSE MODEL

There has been a surge of interest in anisotropic universe models since the release of the 1-year WMAP data in 2003, when several hints of violation of statistical isotropy and/or non-Gaussianity were reported. One such model was devised by ACW in order to study violations of rotational invariance during the inflationary epoch. In this section, we briefly review this model as it will be used as an worked example of the general analysis framework. However, we emphasize that the methods described in this paper are general and suitable for any universe model that predicts a sparse CMB signal covariance matrix.

ACW considered breaking of rotational invariance by generalizing the spectrum of primordial density perturbations  $P(k)$  to include a preferred direction,  $\hat{\mathbf{n}}$ , as well as wave-number  $k$ ,

$$P(\mathbf{k}) = P(k)(1 + g(k)(\hat{\mathbf{k}} \cdot \hat{\mathbf{n}})^2). \quad (1)$$

Here  $\hat{\mathbf{k}}$  is the unit vector along  $\mathbf{k}$ , and  $g(k)$  is a general function of  $k$ . Using a combination of naturalness arguments and detailed analysis of specific models, ACW then argued that  $g(k)$  in most cases can be well approximated by a simple constant,  $g_*$ , and presented the full CMB covariance matrix corresponding to this modified power spectrum,

$$S_{\ell m, \ell' m'} = C_\ell \delta_{\ell \ell'} \delta_{mm'} + \Delta_{\ell m, \ell' m'}. \quad (2)$$

Here  $S_{\ell m, \ell' m'} = \langle a_{\ell m} a_{\ell' m'}^* \rangle$  is the CMB signal covariance matrix,  $C_\ell$  is the angular CMB power spectrum given as

$$C_\ell = \int dk k^2 P(k) \Theta_\ell(k) \Theta_{\ell'}(k) \quad (3)$$

where  $\Theta_\ell(k)$  is the transfer function. The term  $\Delta_{\ell m, \ell' m'}$  is then defined as

$$\begin{aligned} \Delta_{\ell m, \ell' m'} &= g_* \xi_{\ell m, \ell' m'} \int_0^\infty dk k^2 P(k) \Theta_\ell(k) \Theta_{\ell'}(k) \\ &= g_* \xi_{\ell m, \ell' m'} C_{\ell, \ell'}. \end{aligned} \quad (4)$$

In this expression,  $\xi_{\ell m, \ell' m'}$  are geometric coefficients (see ACW for explicit details). The  $\xi$  coefficients couple  $\ell$  to  $\ell' = \{\ell, \ell \pm 2\}$  and  $m$  to  $m' = \{m, m \pm 1, m \pm 2\}$ . All other elements are zero.

The coupling to standard cosmological parameters enter only through  $C_{\ell, \ell'}$ , which is a straightforward generalization of the angular CMB power spectrum. In this paper, we assume that the cosmological parameters are known, and only the anisotropy parameters,  $g_*$  and  $\hat{\mathbf{n}}$ , are unknown. We therefore compute  $C_{\ell, \ell'}$  once, using a very slightly modified version of CAMB (Lewis et al. 2000) that outputs  $C_{\ell, \ell+2}$  in addition to  $C_{\ell, \ell}$ , and adopt this matrix as a prior. We adopt the best-fit  $\Lambda$ CDM model determined from the 5-year WMAP data (Komatsu et al. 2008), and the corresponding  $C_{\ell, \ell}$  and  $C_{\ell, \ell+2}$  elements are plotted in Figure 1. Joint estimation of cosmological parameters and the anisotropy parameters will be considered in a future publication.

In Figure 2 we show one realization drawn from a Gaussian distribution with zero mean and  $S_{\ell m, \ell' m'}$  as covariance matrix, with  $g_* = 0.9999$  (middle row) and  $g_* = -0.9999$  (bottom row) and a preferred direction of  $(l, b) = (0^\circ, 90^\circ)$ . The isotropic signal is depicted in the top row.

The anisotropic contribution alone consists of correlations with the underlying isotropic signal stretched along the plane normal to the preferred direction. The sign of  $g_*$  determines whether the anisotropic contribution is to be added or subtracted from the isotropic signal. If the anisotropic signal is added, then the spots are stretched along the plane normal to the preferred direction. However, if the anisotropic signal is subtracted ( $g_* < 0$ ), then the spots are effectively squeezed along the plane normal to the preferred direction, corresponding to stretching parallel to the preferred direction.

### 2.1. The $A_s - g_*$ degeneracy

From equation (2) and the definition of  $\xi$  (see ACW) it is clear that  $\Delta$  contributes also to the diagonal of the signal covariance matrix, and therefore affects the total angular power spectrum, not only the correlations among  $a_{\ell m}$ 's. This introduces a strong degeneracy between  $g_*$  and the amplitude of the power spectrum of scalar perturbations,  $A_s$  or  $\sigma_8$ . Unless one attempts to estimate the standard  $\Lambda$ CDM parameters jointly with the new anisotropy parameters, one must therefore ensure that a given choice of  $g_*$  does not significantly affect the overall power spectrum, but only the anisotropic contribution.

The diagonal part of  $\Delta$ , for which the integral over the transfer functions equals  $C_\ell$ , is

$$\Delta_{\ell m, \ell m} = g_* C_\ell \xi_{\ell m, \ell m}. \quad (5)$$

The net extra power due to  $\Delta$  is therefore

$$D_\ell = \frac{g_* C_\ell}{2\ell + 1} \sum_{m=-\ell}^{\ell} \xi_{\ell m, \ell m}. \quad (6)$$

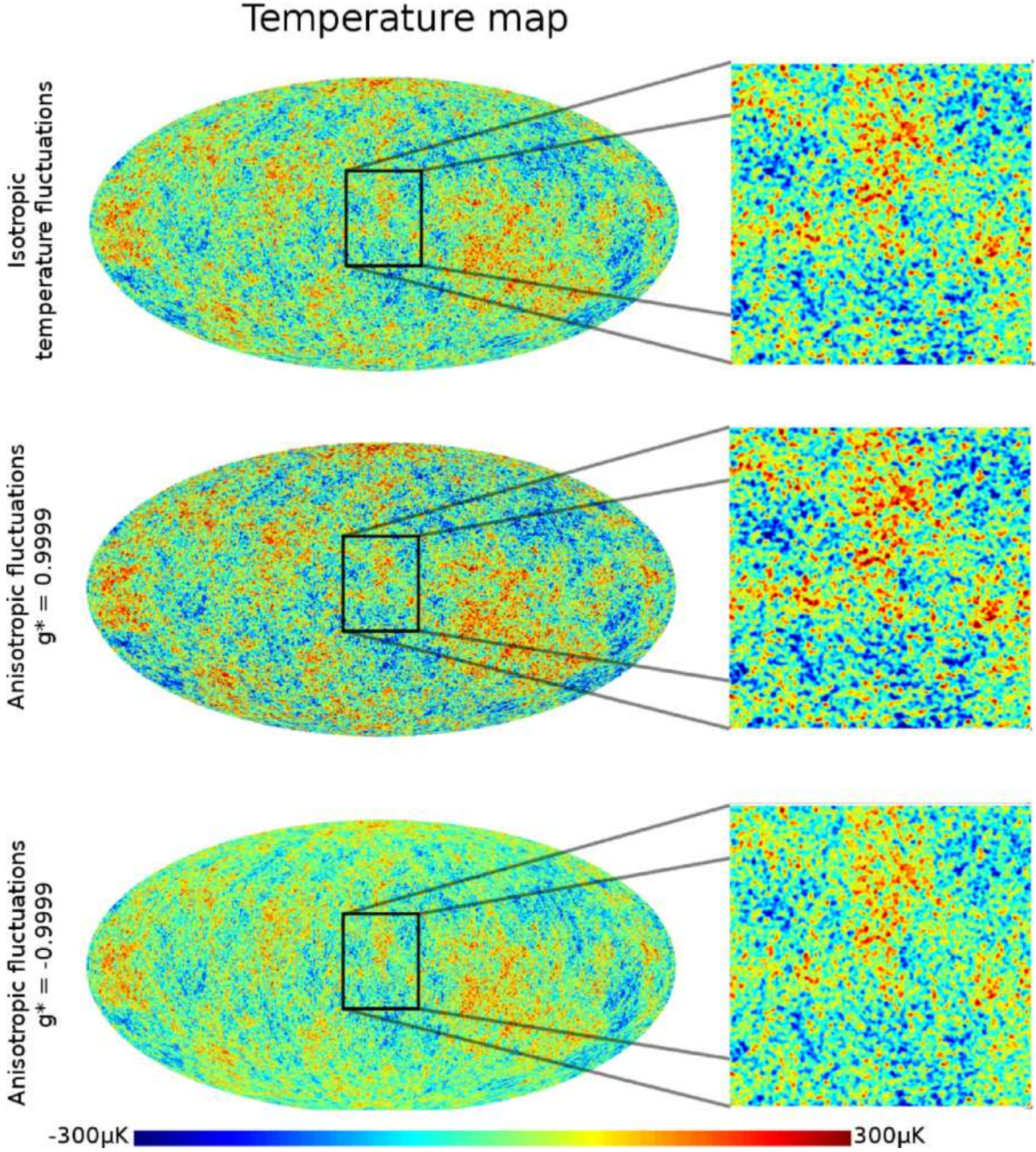


FIG. 2.— Temperature maps showing isotropic fluctuations (top row), while the two lower rows depict anisotropic contributions with  $g_* = 0.9999$  (middle row) and  $g_* = -0.9999$  (bottom row). The maps in the left column are presented in Mollweide projection, while the right row is Cartesian. The anisotropy direction was chosen to be  $(l, b) = (0^\circ, 90^\circ)$ . Note the subtle tendency for stripes along the equator for the positive  $g_*$ , and perpendicular to the equator for negative  $g_*$ .

This may be greatly simplified by considering the detailed form of  $\xi_{\ell m, \ell m}$ ,

$$\xi_{\ell m, \ell m} = -2n_+n_- \frac{-1 + \ell + \ell^2 + m^2}{(2\ell - 1)(2\ell + 3)} + n_0^2 \frac{2\ell^2 + 2\ell - 2m^2 - 1}{(2\ell - 1)(2\ell + 3)}, \quad (7)$$

where

$$n_+ = -\frac{n_x - in_y}{\sqrt{2}}; n_- = \frac{n_x + in_y}{\sqrt{2}}; n_0 = n_z. \quad (8)$$

Averaging this expression over  $m$ , one finds that

$$\frac{1}{2\ell + 1} \sum_{m=-\ell}^{\ell} \xi_{\ell m, \ell m} = \frac{1}{3}, \quad (9)$$

such that  $D_\ell = \frac{1}{3}g_*C_\ell$ . We therefore redefine the total signal covariance matrix to read

$$S_{\ell m, \ell' m'} = \frac{C_\ell \delta_{\ell \ell'} \delta_{mm'} + \Delta_{\ell m, \ell' m'}}{1 + g_*/3}. \quad (10)$$

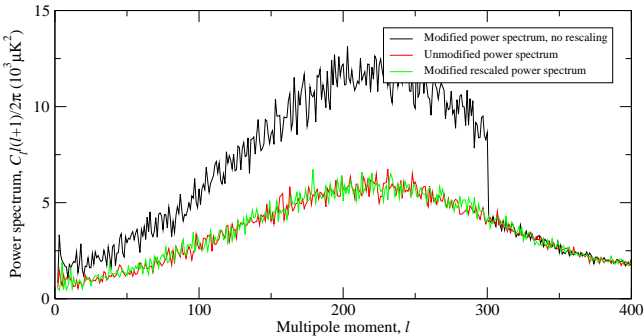


FIG. 3.— Power spectra of simulated anisotropic sky maps with  $g_* = 3$ , with (green) and without (black) rescaling. Red curve shows the power spectrum for an isotropic simulation with  $g_* = 0$ .

With this definition,  $g_*$  is a direct measure of the anisotropic component of  $\mathbf{S}$ , and does not directly depend on the power spectrum  $C_\ell$ .

The effect of  $g_*$  on the power spectrum is demonstrated in Figure 3, where we plot the power spectra of a simulated anisotropic map with  $g_* = 3$ , with and without the above rescaling. Unless proper rescaling is performed, or some equivalent parametrization introduced, it is clear that the strongest constraints on  $g_*$  will come from the observed power spectrum, rather than the correlations among  $a_{\ell m}$ 's.

## 2.2. Posterior analysis and priors

The goal is now to estimate  $g_*$  and  $\hat{\mathbf{n}}$  from observed CMB maps, by computing the posterior distribution  $P(g_*, \hat{\mathbf{n}}|\mathbf{d})$ ,  $\mathbf{d}$  denoting the data. Because we assume that both the noise and CMB sky signal are Gaussian (but anisotropic) random fields, this distribution reads, by Bayes' theorem,

$$P(g_*, \hat{\mathbf{n}}|\mathbf{d}) \propto \mathcal{L}(g_*, \hat{\mathbf{n}})P(g_*, \hat{\mathbf{n}}), \quad (11)$$

where  $\mathcal{L}(g_*, \hat{\mathbf{n}}) = P(\mathbf{d}|g_*, \hat{\mathbf{n}})$  is the likelihood

$$\mathcal{L}(g_*, \hat{\mathbf{n}}) \propto \frac{e^{-\frac{1}{2}\mathbf{d}^T \mathbf{C}^{-1} \mathbf{d}}}{\sqrt{|\mathbf{C}|}} \quad (12)$$

and  $P(g_*, \hat{\mathbf{n}})$  is a prior. Equation (12) can be evaluated in  $\mathcal{O}(N_{\text{pix}}^2)$  operations, as shown by Oh et al. (1999). In this expression,  $\mathbf{C}$  is the signal-plus-noise covariance matrix. In principle, we could now simply map this distribution over a three-dimensional grid, and our task would be completed. However, except for the special case of a data set with uniform noise and full-sky coverage, this is in practice impossible because  $\mathbf{C}$  is a dense matrix, and inversion and matrix determinant therefore scales as  $\mathcal{O}(N_{\text{pix}}^3)$ ,  $N_{\text{pix}}$  being the number of pixels. For current and future data sets, one expects  $N_{\text{pix}} \sim 10^6$  or more.

Fortunately, there is one specific feature of the ACW model that does make an exact analysis possible: Although the *full-sky* CMB covariance matrix is non-diagonal, it is not dense. Rather, it has a well-defined shape in harmonic space ( $\ell$  is coupled to  $\ell' = \{\ell, \ell \pm 2\}$  and  $m$  to  $m' = \{m, m \pm 1, m \pm 2\}$ ) that allows for cheap matrix storage and fast Cholesky decomposition. This, combined with the development of the standard diagonal CMB Gibbs sampler mentioned in the introduction (Jewell et al. 2004; Wandelt et al. 2004; Eriksen et al. 2004b), allows us to perform a full proper analysis, as explained in the next section.

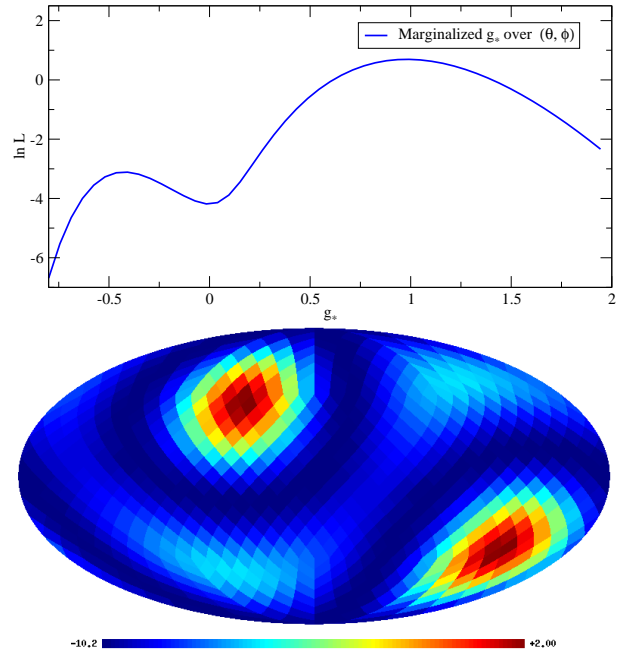


FIG. 4.— Marginal likelihood functions for  $\mathcal{L}(g_*)$  (top) and  $\mathcal{L}(\hat{\mathbf{n}})$  (bottom) for a simulated data set with uniform noise and full-sky coverage, shown in logarithmic units. The input values of  $g_* = 0.8$  and  $(l, b) = (57^\circ, 33^\circ)$  are accurately reproduced. Notice the shallow local maximum at  $g_* \sim -0.5$  and the secondary peaks in the marginal direction map.

Before describing this method, we consider first the special case of data having uniform noise and full-sky coverage, which is useful to illustrate the approach, and highlight some particular issues. For this particular case, the full data covariance matrix, expressed in spherical harmonic space, has the same sparse filling pattern as the ACW covariance matrix, and direct evaluation is therefore possible using sparse matrix techniques (e.g., Davis 2005).

We simulated a single CMB realization from the ACW model, adopting a high anisotropy amplitude of  $g_* = 0.8$  and a preferred direction (in Galactic longitude and latitude) of  $(l, b) = (57^\circ, 33^\circ)$ , then convolved this realization with a  $90'$  FWHM Gaussian beam, and projected it onto a HEALPix<sup>3</sup> grid with resolution parameter  $N_{\text{side}} = 128$ . Finally, uniform, Gaussian noise with  $10\mu\text{K}$  RMS was added to each pixel. This simulation was then analyzed by computing the raw likelihood over a three-dimensional grid, and finally marginalized likelihoods were produced by numerical integration. The results from this exercise is shown in Figure 4.

As expected, the likelihood peaks close to the input values. However, there is also a second local maximum at  $g_* \sim -0.5$  with a direction of  $(l, b) \sim (45^\circ, -50^\circ)$ ,  $90^\circ$  with respect to the main axis. This maximum becomes visible only for large negative values of  $g_*$ . The existence of this maximum becomes intuitive when considering figure 2: Flipping the sign of  $g_*$  and rotating the preferred axis by  $90^\circ$  leads to stripes in the same direction as the original parameters.

This is not a significant issue for a direct evaluation method, since the local maximum has a very small amplitude. (Note that the marginal likelihoods in Figure

<sup>3</sup> <http://healpix.jpl.nasa.gov>

4 are shown in logarithmic units.) However, for MCMC methods it can cause problem in terms of burn-in: As explained in the next section, our method is based on the well-known MCMC and Gibbs sampling algorithms, and these essentially correspond to performing a random walk on the likelihood surface. Further, each chain is initialized randomly on the sphere. It is therefore a significant chance that a number of chains may get trapped in a local maximum, and thereby bias the final posterior. To avoid this, we impose a uniform prior of  $g_* \geq -0.2$  in this paper, and a uniform prior on the sphere for  $\hat{\mathbf{n}}$ . If the final posteriors from the actually WMAP analysis happened to peak close to  $g_* = -0.2$  we would have to re-consider this choice more carefully, but as we shall see, this is not the case.

### 3. METHOD

We now discuss the method for mapping out the desired posterior. This method is a very slight generalization of the previously described CMB Gibbs sampler developed by Jewell et al. (2004), Wandelt et al. (2004) and Eriksen et al. (2004b), which was originally intended for power spectrum estimation. The underlying Gibbs sampler implementation used for this work is the code called “Commander”, described in detail by Eriksen et al. (2004b, 2008a).

#### 3.1. Review of the CMB Gibbs sampler

We first review the CMB Gibbs sampler as previously described in literature. In any Bayesian analysis, a main goal is the posterior distribution  $P(\theta|\mathbf{d})$ , where  $\theta$  is a set of parameters connected to some model and  $\mathbf{d}$  are the observed data. For high-dimensional spaces, brute-force evaluations of the posterior are computationally unfeasible, and one usually resorts to Monte Carlo Markov chain (MCMC) methods.

##### 3.1.1. Notation and data model

We begin by defining a parametric model for the CMB observations. Given our current understanding of the CMB sky, the observed data may be accurately modelled as a sum of a CMB anisotropy term and a noise term,

$$\mathbf{d} = \mathbf{As} + \mathbf{n}. \quad (13)$$

Here  $\mathbf{d}$  represents the observed data,  $\mathbf{A}$  denotes convolution by an instrumental beam,  $\mathbf{s}(\theta, \phi) = \sum_{\ell,m} a_{\ell m} Y_{\ell m}(\theta, \phi)$  is the CMB sky signal represented in either harmonic or real space, and  $\mathbf{n}$  is instrumental noise.

Further, it is a good approximation to assume both the CMB and noise to be zero mean Gaussian distributed variates, with covariance matrices  $\mathbf{S}$  and  $\mathbf{N}$ , respectively. In harmonic space, the signal covariance matrix is defined by  $\mathbf{S}_{\ell m, \ell' m'} = \langle a_{\ell m} a_{\ell' m'}^* \rangle$ , which may or may not be diagonal. The connection to cosmological parameters  $\theta$  is made through this covariance matrix. Finally, for experiments such as WMAP, the noise is often assumed uncorrelated between pixels,  $\mathbf{N}_{ij} = \sigma_i^2 \delta_{ij}$ , for pixels  $i$  and  $j$ , and noise RMS equals to  $\sigma_i$ .

Our goal is now to compute the full joint posterior  $P(\theta|\mathbf{d})$ , which, as already mentioned, is given by  $P(\theta|\mathbf{d}) \propto P(\mathbf{d}|\theta)P(\theta) = \mathcal{L}(\theta)P(\theta)$ , where  $\mathcal{L}(\theta)$  is the likelihood, and  $P(\theta)$  is a prior. For a Gaussian data

model, the likelihood is

$$\mathcal{L}(\theta) \propto \frac{e^{-\frac{1}{2}\mathbf{d}^T \mathbf{C}^{-1}(\theta) \mathbf{d}}}{\sqrt{|\mathbf{C}(\theta)|}}. \quad (14)$$

#### 3.1.2. Posterior mapping by Gibbs sampling

When working with real-world CMB data, there are a number of issues that complicate the analysis. Two important examples are anisotropic noise and Galactic foregrounds. First, because of the scanning motion of a CMB satellite, the pixels in a given data set are observed by unequal amounts of time. This implies that the effective noise is a function of position on the sky. Second, large regions of the sky are obscured by Galactic foregrounds (e.g., synchrotron, free-free and dust emission), and these regions must be rejected from the analysis by masking.

Because of these issues, the total data covariance matrix  $\mathbf{S} + \mathbf{N}$  is dense in both pixel and harmonic space. As a result, it is computationally difficult to evaluate the likelihood in Equation (14), since the computational cost of matrix inversion and determinant evaluation scale as  $\mathcal{O}(N_{\text{pix}}^3)$ . Fortunately, this problem has already been solved for the CMB context, through the development of the CMB Gibbs sampler.

The idea behind the CMB Gibbs sampler is to estimate the CMB sky,  $\mathbf{s}$ , together with the covariance parameters, by computing  $P(\theta, \mathbf{s}|\mathbf{d})$ , and then subsequently marginalize over  $\mathbf{s}$ . Specifically, the algorithm is the following: First choose any initial guess,  $(\theta, \mathbf{s})^0$ . Then alternately sample from each of the *conditional* distributions,

$$\theta^{i+1} \leftarrow P(\theta|\mathbf{s}^i, \mathbf{d}) \quad (15)$$

$$\mathbf{s}^{i+1} \leftarrow P(\mathbf{s}|\theta^{i+1}, \mathbf{d}). \quad (16)$$

The theory of Gibbs sampling then guarantees that the joint samples  $(\theta, \mathbf{s})^i$  will, after some burn-in period, be drawn from the desired joint distribution. The remaining step is then simply to formulate sampling algorithms for each of the two conditionals,  $P(\theta|\mathbf{s}, \mathbf{d})$  and  $P(\mathbf{s}|\theta, \mathbf{d})$ .

We first consider  $P(\mathbf{s}|\theta, \mathbf{d})$ . This may, under the assumption of Gaussianity, be written as

$$P(\mathbf{s}|\theta, \mathbf{d}) = P(\mathbf{d}|\mathbf{s}, \theta)P(\mathbf{s}|\theta) \quad (17)$$

$$\propto e^{-\frac{1}{2}(\mathbf{d}-\mathbf{s})^T \mathbf{N}^{-1}(\mathbf{d}-\mathbf{s})} e^{-\frac{1}{2}\mathbf{s}^T \mathbf{S}^{-1} \mathbf{s}} \quad (18)$$

$$= e^{-\frac{1}{2}(\mathbf{s}-\hat{\mathbf{s}})^T (\mathbf{S}^{-1} + \mathbf{N}^{-1})(\mathbf{s}-\hat{\mathbf{s}})}, \quad (19)$$

where we have defined the Wiener filtered map,  $\hat{\mathbf{s}} = (\mathbf{S}^{-1} + \mathbf{N}^{-1})^{-1} \mathbf{N}^{-1} \mathbf{d}$ . Thus,  $P(\mathbf{s}|\theta, \mathbf{d})$  is a Gaussian distribution with mean  $\hat{\mathbf{s}}$  and covariance  $(\mathbf{S}^{-1} + \mathbf{N}^{-1})^{-1}$ .

Sampling from this distribution is straightforward, but implementationally somewhat involved: Draw two Gaussian random maps,  $\eta_0$  and  $\eta_1$ , with zero mean and unit variance, and solve the following equation for  $\bar{\mathbf{s}}$ ,

$$(\mathbf{S}^{-1} + \mathbf{N}^{-1})\bar{\mathbf{s}} = \mathbf{N}^{-1}\mathbf{d} + \mathbf{L}^{-T}\eta_0 + \mathbf{N}^{-\frac{1}{2}}, \quad (20)$$

where  $\mathbf{L}$  is the Cholesky decomposition of  $\mathbf{S} = \mathbf{LL}^T$ . By multiplying both sides of this equation with  $(\mathbf{S}^{-1} + \mathbf{N}^{-1})^{-1}$ , one immediately sees that  $\langle \bar{\mathbf{s}} \rangle = \hat{\mathbf{s}}$ , and a few more computations show that  $\langle (\bar{\mathbf{s}} - \hat{\mathbf{s}})(\bar{\mathbf{s}} - \hat{\mathbf{s}})^T \rangle = (\mathbf{S}^{-1} + \mathbf{N}^{-1})^{-1}$ , as required.

For improved numerical stability, this linear system is in practice rewritten into the following form,

$$(1 + \mathbf{L}^T \mathbf{N}^{-1} \mathbf{L})(\mathbf{L}^{-1} \bar{\mathbf{s}}) = \mathbf{L}^T \mathbf{N}^{-1} \mathbf{d} + \eta_0 + \mathbf{L}^T \mathbf{N}^{-\frac{1}{2}}, \quad (21)$$

which is first solved for  $\mathbf{x} = \mathbf{L}^{-1}\bar{\mathbf{s}}$  by conjugate gradients, and then for  $\bar{\mathbf{s}} = \mathbf{L}\mathbf{x}$ . For further implementational details, see, e.g., Eriksen et al. (2008a). Note, however, that in previous papers equation (21) was always written with symmetric signal covariance square roots,  $\mathbf{S}^{\frac{1}{2}} = (\mathbf{S}^{\frac{1}{2}})^T$ . The current form is based on the Cholesky decomposition, which is computationally considerably cheaper than the symmetric form, especially for sparse matrices.

Finally, we need a sampling algorithm for  $P(\theta|\mathbf{s}, \mathbf{d})$ . In previous publications, the main emphasis has been on covariance matrices parametrized by the angular CMB power spectrum,  $C_{\ell m, \ell' m'} = C_\ell \delta_{\ell\ell'} \delta_{mm'}$ . In this case,  $P(C_\ell|\mathbf{s}, \mathbf{d})$  reduces to a simple inverse Gamma distribution, for which there is a simple textbook sampling algorithm available. As the details of this specific algorithm is of little use for the application presented here, we refer the interested reader to earlier papers for full details on this procedure, e.g., Wandelt et al. (2004) or Eriksen & Wehus (2008).

### 3.2. Gibbs sampling with non-diagonal covariances

We now describe the two modifications to the CMB Gibbs sampler that allow us to analyze models with non-diagonal covariances. This involves adding support for non-diagonal covariance matrices for  $P(\mathbf{s}|\theta, \mathbf{d})$  and implementing a more general sampling algorithm for  $P(\theta|\mathbf{s}, \mathbf{d})$ .

#### 3.2.1. Sampling from $P(\mathbf{s}|\theta, \mathbf{d})$

We first consider sampling of sky maps,  $\mathbf{s}$ , given a set of cosmological parameters,  $\theta$ , and the associated covariance matrix  $\mathbf{S}(\theta)$ . Formally, the sampling algorithm for  $P(\mathbf{s}|\theta, \mathbf{d})$  is identical to that given by equation (21). However, in this case  $\mathbf{S}$  is a non-diagonal matrix and the computational complexity is therefore greatly increased. Only special cases can be considered, for instance models that predict a sparse covariance matrix. This is the case for the ACW model.

For general dense anisotropic covariance matrices, the memory requirements scale as  $\mathcal{O}(\ell_{\max}^4)$ , effectively rendering studies of anisotropic models where  $\ell_{\max} \gtrsim 100$  impossible. However, working only with sparse matrices, the memory consumption scales as  $\mathcal{O}(\ell_{\max}^2)$ , enabling calculations of covariance matrices with  $\ell_{\max}$  well into the Planck regime ( $\ell_{\max} \sim 2500$ ).

To be able to handle sparse matrices efficiently, we have ported the LDL library of Davis (2005) to Fortran 90, and incorporated this into Commander. This library stores sparse matrices in a packed format, and supports fast Cholesky decomposition. Our F90 version of LDL may be obtained by sending an email to the authors, and will be released publicly at a later time.

In the present paper, we are primarily concerned with the ACW model, and the corresponding covariance matrix exhibits correlations between  $\ell$  and  $\ell' = \{\ell, \ell \pm 2\}$  and between  $m$  and  $m' = \{m, m \pm 1, m \pm 2\}$ . Thus, the number of elements up to  $\ell_{\max}$  is  $\mathcal{O}(15\ell_{\max}^2)$ . For example, for  $\ell_{\max} = 300$  the memory requirements are  $\sim 14\text{Mb}$  with double precision complex numbers. Since the covariance matrix is very sparse, the CPU time required for Cholesky decomposition is nearly linear in  $\ell_{\max}^2$ .

We define three different harmonic space limits in our code, namely  $\ell_{\max}$ ,  $\ell_{\text{low}}$  and  $\ell_{\text{high}}$ . The former denotes

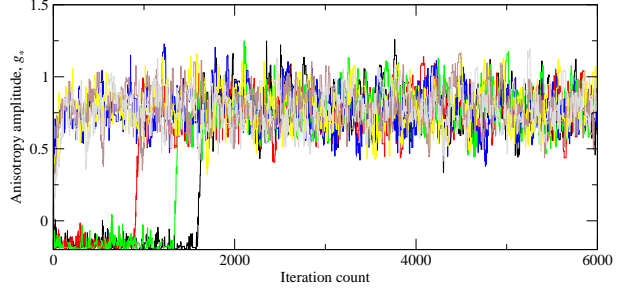


FIG. 5.— Evolution of Gibbs chains mapping the posterior of a simulated data set. Note how chains trapped in the local maximum at negative anisotropy amplitude eventually converges to the positive maximum.

the maximum multipole moment of the full spherical harmonics composition used in the analysis, while the latter two denotes the range in which the anisotropic covariance matrix is used. In addition, we remove the monopole and dipole from the analysis. Thus, the total covariance matrix reads

$$S_{\ell m, \ell' m'} = \begin{cases} 0 & \ell, \ell' \leq 1 \\ C_\ell \delta_{\ell\ell'} \delta_{mm'} & 2 \leq \ell, \ell' < \ell_{\text{low}} \\ \frac{(C_\ell \delta_{\ell\ell'} \delta_{mm'} + \Delta_{\ell m, \ell' m'})}{1+g_*/3} & \ell_{\text{low}} \leq \ell, \ell' \leq \ell_{\text{high}} \\ C_\ell \delta_{\ell\ell'} \delta_{mm'} & \ell_{\text{high}} < \ell, \ell' \leq \ell_{\max} \end{cases} \quad (22)$$

The reason for defining  $\ell_{\min}$  and  $\ell_{\max}$  as free parameters is that it may be useful to study the dependence of  $\theta$  on a particular  $\ell$ -range. On the other hand, this implies that the model implemented in this paper is only an approximation to the full ACW model, for which the correlations extend over all  $\ell$ 's, and is only exact when  $\ell_{\text{high}} = \ell_{\max}$ .

With the sparse matrix operations implemented, the algorithm is precisely the same as for the diagonal case, and both rely on the solution of a linear system by Conjugate Gradients (CG; Eriksen et al. 2004b). In order to achieve an acceptable CG convergence rate, it is therefore necessary to establish a good preconditioner. However, as long as the off-diagonal elements remain small, the standard diagonal covariance matrix preconditioner performs reasonably even for the off-diagonal case. For the present paper, we therefore adopt the same preconditioner as described by Eriksen et al. (2004b), which consists of the directly inverted full matrix evaluated up to some  $\ell_{\text{precond}}$ , and then a strictly diagonal matrix from  $\ell_{\text{precond}} + 1$  to  $\ell_{\max}$ .

The number of CG iterations per map making step is typically 70 for a WMAP-type run, and with a total CPU time per iteration of about 15 seconds, the total cost for a single sample is  $\sim 20$  CPU minutes. The average CPU time required to set up and perform a Cholesky decomposition of the corresponding covariance matrix for  $\ell_{\max} = 512$ ,  $\ell_{\text{low}} = 2$  and  $\ell_{\text{high}} = 300$  is  $\sim 20$  seconds.

#### 3.2.2. Sampling from $P(\theta|\mathbf{s}, \mathbf{d})$

Finally, we have to formulate a sampling algorithm for  $P(\theta|\mathbf{s}, \mathbf{d})$ . Recall that for the diagonal power spectrum case, this step is typically performed by a standard inverse Gamma distribution sampler (e.g., Gupta & Nagar 2000; Eriksen & Wehus 2008). For the general case considered here, we adopt a standard Metropolis MCMC sampler (e.g., Liu 2001).

First, note that  $P(\theta|\mathbf{s}, \mathbf{d}) = P(\theta|\mathbf{s})$ ; if we already know

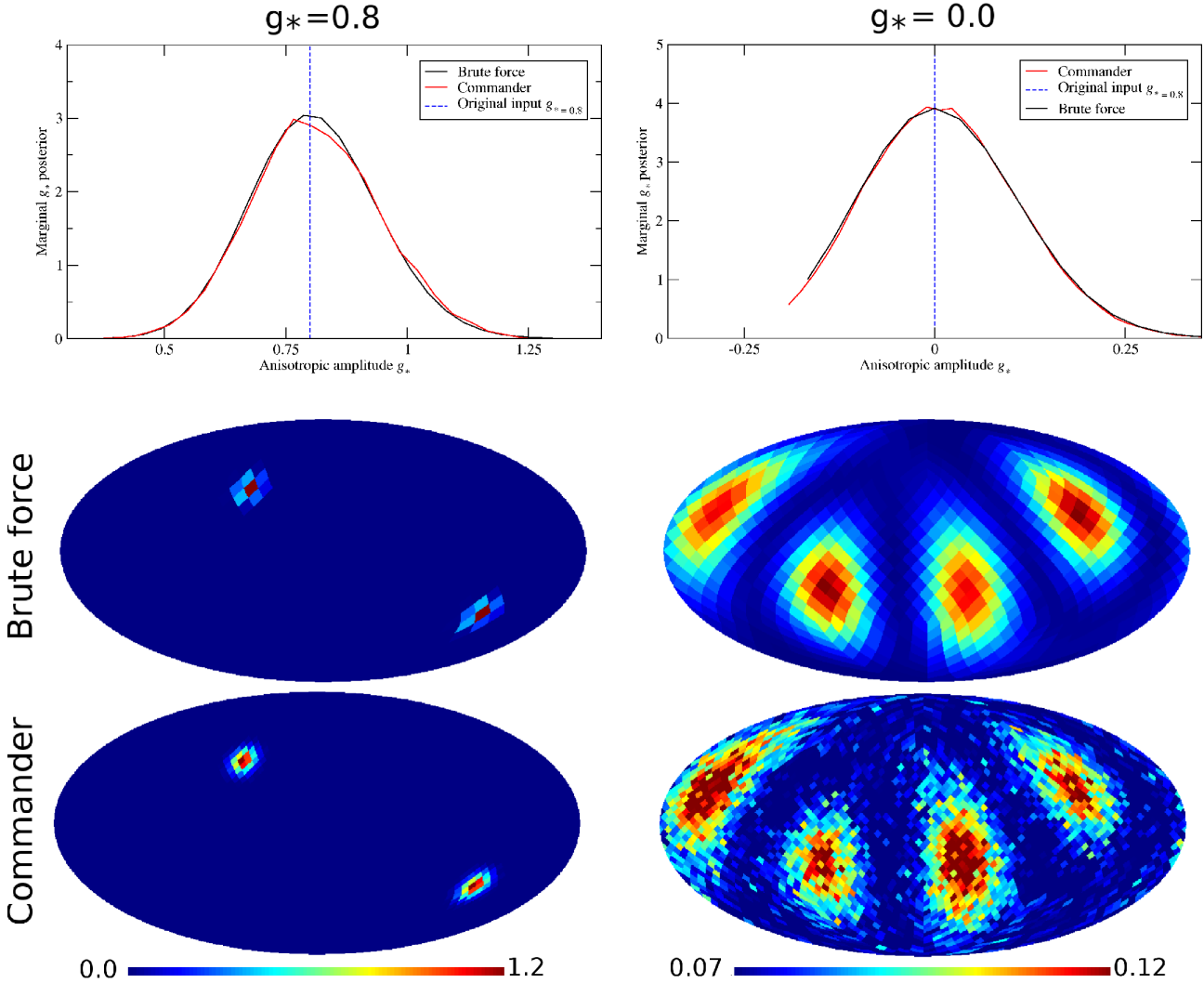


FIG. 6.— Posterior distributions for simulated maps with a significant anisotropic amplitude  $g_* = 0.8$  (left) and no anisotropic amplitude  $g_* = 0.0$  (right). Note how the anisotropic input parameters  $\theta, \phi, g_*$  were successfully reproduced.

the CMB sky perfectly, no additional data can possibly tell us anything more about the anisotropy parameters  $\theta$ . Second, although the CMB sky is now manifestly anisotropic, we still assume that it is Gaussian, and the target distribution therefore reads

$$P(\theta|\mathbf{s}) \propto \frac{e^{-\frac{1}{2}\mathbf{s}^T \mathbf{S}^{-1} \mathbf{s}}}{\sqrt{|\mathbf{S}|}}. \quad (23)$$

For sparse matrices, this may be directly evaluated by first computing the Cholesky decomposition of  $\mathbf{S} = \mathbf{L}\mathbf{L}^T$ , and then, on the one hand, solve for  $\mathbf{x} = \mathbf{L}\mathbf{s}$ , and on the other hand, compute  $|\mathbf{S}| = |\mathbf{L}|^2$ .

We adopt a simple symmetric proposal rule for the Metropolis sampler, and the acceptance probability therefore simply reads

$$p = \frac{P(\theta^p|\mathbf{s})}{P(\theta^i|\mathbf{s})}, \quad (24)$$

where  $\theta^p$  is the proposed sample and  $\theta^i$  is the current sample of the MCMC chain. Specifically, we adopt a Gaussian proposal density for  $g_*$  and a uniform proposal over a disk for  $\hat{\mathbf{n}}$ , centered on the current state. The proposal density is typically tuned by producing a short test

chain before the main run, such that the final observed acceptance rate lies between 0.2 and 0.7.

Finally, because the computational cost is much lower for this step than for  $P(\mathbf{s}|\theta, \mathbf{d})$ , we produce several  $\theta$  samples per main Gibbs iteration, to improve the convergence properties of the chain. This essentially corresponds to performing a partial Rao-Blackwellization (Chu et al. 2005). A typical number of MCMC samples per main Gibbs iteration is 30.

#### 4. APPLICATIONS TO SIMULATED DATA

We now apply the methods described above to simulated data, both in order to validate the code and to build up intuition about the target distribution. Note that the discussion from now on specializes exclusively to the ACW model, and it is possible that other technical issues than those described here may arise when considering other models. Burn-in, mixing and convergence are issues that must be considered on a case-to-case basis.

##### 4.1. Simulations

To test our implementation and study the behavior of the algorithm in general, we simulate a few different maps from the ACW model, and analyze these maps with

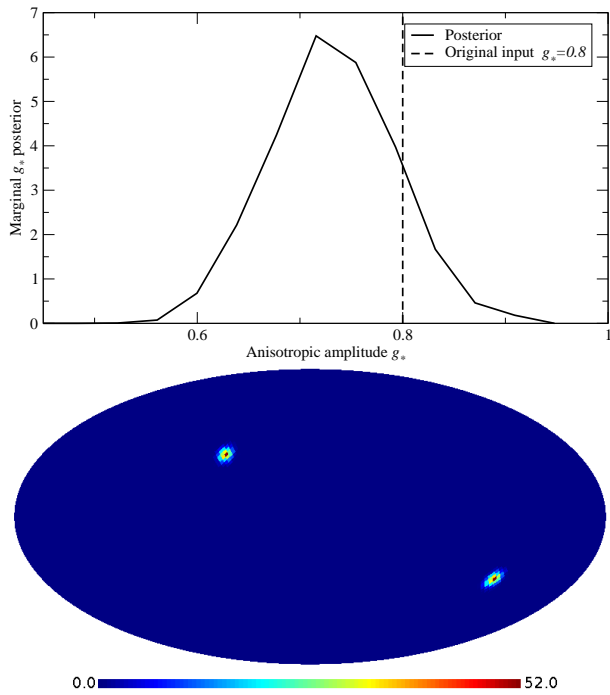


FIG. 7.— Posterior distributions for a simulated WMAP data set, using the V-band beam, V band RMS noise and the KQ85 sky cut.

our modified Gibbs sampler. The CMB component of these maps is made by generating a random vector,  $\eta$ , of Gaussian uniform variates with zero mean and unit variance, and then computing  $\mathbf{s} = \mathbf{L}\eta$ . This realization is then convolved with a beam function and the HEALPix pixel window, before it is projected on a HEALPix grid. Finally, Gaussian noise is added to each pixel.

The first two simulations have a resolution of  $N_{\text{side}} = 128$ ,  $\ell_{\text{max}} = 256$ ,  $\ell_{\text{low}} = 2$ ,  $\ell_{\text{high}} = 200$  and a Gaussian beam of  $90'$  FWHM. The noise RMS is  $10 \mu\text{K}$  uniformly over the full sky. The first of the two simulations has an anisotropy amplitude of  $g_* = 0.8$  and a preferred direction towards  $(l, b) = (57^\circ, 33^\circ)$ , and the other  $g_* = 0$ . These two simulations are primarily used to compare the Gibbs sampler with brute-force likelihood evaluation, which is only possible for uniform noise and full-sky coverage.

Second, we generate a full WMAP5 like simulation based on the V1 differencing assembly (DA), with  $g_* = 0.8$ ,  $N_{\text{side}} = 512$ ,  $\ell_{\text{max}} = 600$ ,  $\ell_{\text{low}} = 2$ ,  $\ell_{\text{high}} = 300$  and beam and noise properties appropriate for the V1 DA<sup>4</sup>. In this case, we also apply the KQ85 sky cut (Gold et al. 2008), which removes 18% of the sky. This simulation is used to verify that correct results are obtained for realistic WMAP data, including anisotropic (but uncorrelated) noise and a sky cut.

#### 4.2. Burn-in and convergence

We first consider the issue of burn-in and convergence, and analyze the simulation with  $g_* = 0.8$ , uniform noise and full-sky coverage. In Figure 5 we show the first 6000  $g_*$  samples produced by each of 14 chains. First, notice that the chains immediately divide into two classes, one which converges quickly towards  $g_* \sim 0.8$  and one which

hovers near the lower prior of  $g_* = -0.2$ . This is due to the fact that the chains are initialized randomly on the sphere, and those that happen to start close to the non-physical local maximum (see Section 2.2) get temporarily trapped in this local maximum. However, as the chains explores the likelihood surface, they are able to converge into the right regime, and find the correct value. In this case, all chains have reached the equilibrium state after 1800 iterations. The pre-burn-in samples must be rejected from the further analysis. For now, we inspect each chain individually, to make sure that they have all reached the common state.

Note that there is a fundamental difference between low and high signal-to-noise cases in this respect: If  $g_*$  is low, the chains may jump between local maxima, while if  $g_*$  is high, some chains typically start out in the global maximum and stay there, while others start in the local maximum, and eventually converge into the right regime. Which situation is relevant for a particular data set must be considered on a case-by-case basis, by checking whether the chains jump between states, or if they stay in one place. It is also advisable to run many chains in parallel, randomly initialized over the full sphere, to understand how many local maxima the distribution has.

Second, once the chains have burned in, we must also ensure that they collectively have converged to the full posterior. One possible measure for this is the Gelman-Rubin  $R$  statistic (e.g., Gelman & Rubin 1992; Eriksen et al. 2006), which compares the variances within a single chain with the variance between chains. If the chains have converged properly,  $R$  should be close to unity. Typically, one recommends that  $R$  should be less than 1.1 or 1.2. For the chains shown in Figure 5, we find that  $R = 1.01$  after rejecting the first 2000 burn-in samples, indicating very good convergence. Considering further subsets of these samples, we find that 5000 samples is sufficient to achieve  $R < 1.1$  and 20 000 samples for  $R < 1.02$ . In the analyses presented later, we always have more than 20 000 samples.

#### 4.3. Validation

We now analyze the two simulations with uniform noise and full-sky coverage, having  $g_* = 0$  and  $g_* = 0.8$ , respectively. In addition to running the Gibbs sampler on these simulations, we also compute the full three-dimensional likelihood function over a grid in  $(g_*, \hat{\mathbf{n}})$ , and numerically integrate to produce brute-force marginal posteriors.

The resulting distributions are shown in Figure 6; the left column shows the  $g_* = 0.8$  case, and the right column shows the  $g_* = 0$  case. We see, as expected, that the two methods produce identical results, up to sampling uncertainty and grid resolution. Note that this holds both for high and low anisotropy amplitudes, indicating that the method is robust in all regimes.

Next, we see that when the amplitude is large, there is only one visible preferred direction in the direction posterior; the secondary direction is too shallow to be seen. On the other hand, there are two “preferred” directions in the  $g_* = 0$  case. However, the span in likelihood over the full sphere is in this case only a factor of two between the least and most preferred directions, which essentially indicates a uniform distribution.

In Figure 7 we show similar plots for the WMAP simulation with uncorrelated noise, based on the V1 differenc-

<sup>4</sup> <http://lambda.gsfc.nasa.gov>

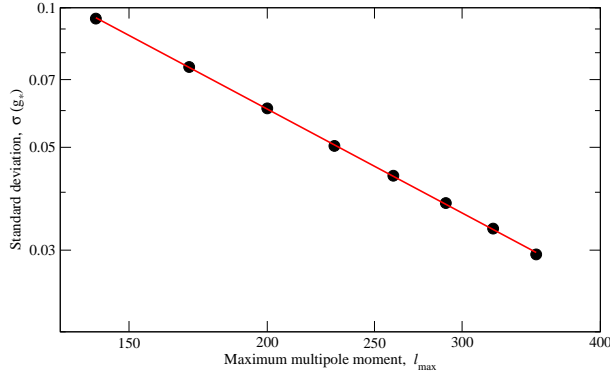


FIG. 8.— Estimated uncertainty in  $g_*$  as a function of  $\ell_{\text{high}}$  (black dots) and a best-fit power law function (red line) for cosmic variance limited data  $g_* = 0.8$ . In this case it is not possible to evaluate the likelihood directly, since the noise is inhomogeneous and there is a sky cut. Still, we see that correct results are obtained. This concludes the verification of both the method and our implementation, and we are now ready to analyze the five-year WMAP temperature sky maps.

#### 4.4. Forecasts for cosmic variance limited data

Before turning to the analysis of the actual WMAP data, we compute the uncertainty in  $g_*$  as a function of  $\ell_{\text{high}}$  for full-sky noiseless data. (The lower limit is always kept at  $\ell_{\text{low}} = 2$ .) This topic was also considered by Pullen & Kamionkowski (2007), who presented both a more general formalism and forecasts for specific experiments. Note, however, that our parametrization is slightly different from theirs, as we introduce a rescaling of the covariance matrix to eliminate the power spectrum degeneracy (Section 2.1).

We carry out this analysis by simulating anisotropic ACW maps with  $g_* = 0$  and different  $\ell_{\text{high}}$ , and analyze these with the brute-force evaluation approach described above. No noise or beam effects are included. For each case, we marginalize over  $\hat{\mathbf{n}}$  to obtain  $P(g_*|\mathbf{d})$ , and compute the standard deviation,  $\sigma(g_*)$ , from this distribution.

Figure 8 shows  $\sigma(g_*)$  as a function of  $\ell_{\text{high}}$ . From this figure, we see that  $\sigma(g_*)$  is very close to a power law in  $\ell_{\text{high}}$ , in good agreement with the arguments given by Pullen & Kamionkowski (2007). The best-fit power law function is

$$\sigma(\ell_{\text{high}}; g_*) = 0.025 \left( \frac{\ell_{\text{high}}}{400} \right)^{-1.27}, \quad (25)$$

and this can be used to produce rough forecasts for various experiments. For instance, in this paper we conservatively adopt  $\ell_{\text{high}} = 400$  for the WMAP analysis, to avoid possibly complicating high- $\ell$  issues such as point source confusion and noise mis-estimation. In that case, we expect an uncertainty of  $\sigma(g_*) = 0.025$ , before taking into account noise and sky cut. This is in excellent agreement with the  $\sigma(g_*) = 0.024$  result of Pullen & Kamionkowski (2007), derived with slightly different data and model assumptions and a completely different approach.

#### 5. APPLICATION TO THE FIVE-YEAR WMAP DATA

We now analyze the five-year WMAP data, and present the full marginal  $P(g_*|\mathbf{d})$  and  $P(\hat{\mathbf{n}}|\mathbf{d})$  posteriors for various data cuts.

#### 5.1. Data

In this paper, we consider the five-year WMAP temperature sky maps (Hinshaw et al. 2008), and analyze the V- and W-bands (61 and 94 GHz), which are believed to be the cleanest WMAP bands in terms of residual foregrounds. We adopt the template-corrected, foreground reduced maps recommended by the WMAP team for cosmological analysis, and impose both the KQ75 and KQ85 masks (Gold et al. 2008), which remove 28% and 18% of the sky, respectively. Point source cuts are imposed in both cases.

We mainly analyze the data frequency-by-frequency, and consider the combinations V1+V2 and W1 through W4. In addition, we compute the posteriors for V1 and V2 separately. The noise RMS patterns and beam profiles are taken into account for each DA individually. The noise is assumed uncorrelated between pixels and bands. For details on joint Gibbs analysis of multi-frequency data, see Eriksen et al. (2004b). All data used in this analysis are available from LAMBDA.

The angular resolutions of the V- and W-bands are  $0.35^\circ$  and  $0.22^\circ$ , respectively, and the sky maps are pixelized at a HEALPix resolution of  $N_{\text{side}} = 512$  with  $7'$  pixels. We therefore adopt a harmonic space cutoff of  $\ell_{\text{max}} = 700$  and 800 for the two data sets, probing deeply into the noise dominated regime. However, we never consider multipoles at  $\ell > 400$  for the anisotropic part of the signal covariance matrix, in order to minimize the chance of systematic effects such as residual point source contributions, beam uncertainties or noise mis-estimation to affect our results. See Table 1 for a list of the specific  $\ell$ -ranges considered.

We also note that the maps studied here are cleaned using external templates (Gold et al. 2008), which must be considered a fairly rough approach to foreground cleaning. A better approach is to use the joint foreground and CMB Gibbs sampler (Eriksen et al. 2008a), which provides the user with a CMB map marginalized over very general foreground models. This work is currently underway for the five-year WMAP data, and the results will be reported elsewhere (Dickinson et al., in preparation). However, as an explicit foreground test we also analyze the raw V-band data, from which no foreground templates have been subtracted, and find very consistent results.

#### 5.2. Results

We now present the marginal posteriors for the ACW model obtained from the five-year WMAP temperature sky maps, as computed with the method described in §3. First, in the top row of Figure 9 we show the marginal anisotropy amplitude posterior,  $P(g_*|\mathbf{d})$ , for V- (left column) and W-band (right column), and in the three bottom rows we show the preferred direction posteriors,  $P(\hat{\mathbf{n}}|\mathbf{d})$ . In Table 1 the full set of results are summarized quantitatively.

First, we see that there is an apparently clear detection of  $g_* \neq 0$  when considering the full range of multipoles,  $\ell = [2, 400]$ . The W-band posterior has  $g_* = 0.15 \pm 0.04$ , nominally corresponding to a  $3.8\sigma$  detection, and the V-band posterior has  $g_* = 0.10 \pm 0.04$ , internally consistent with W-band at  $\sim 1\sigma$ . Second, the direction posteriors indicate a clearly preferred direction pointing towards

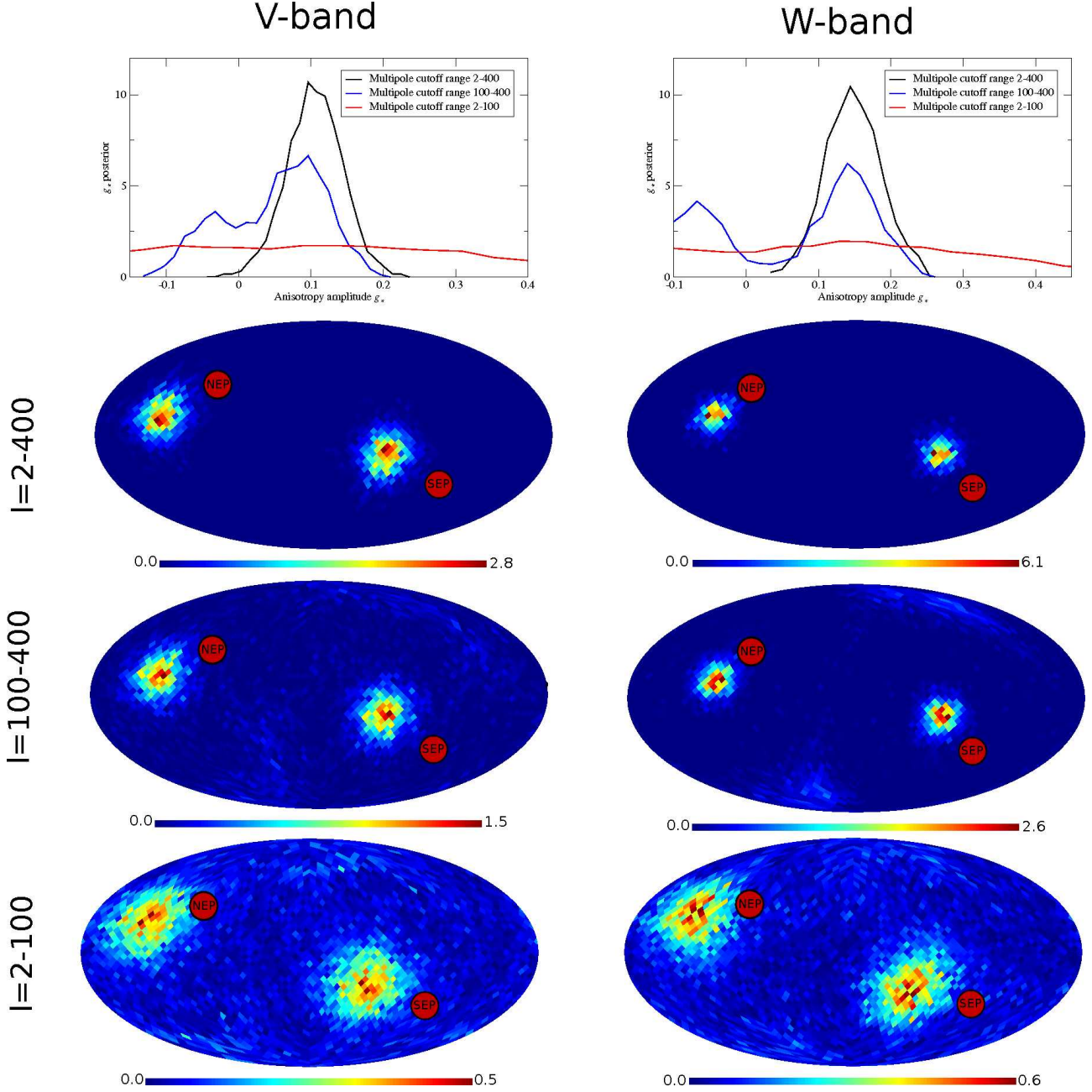


FIG. 9.— Marginal ACW posteriors obtained from the V- (left) and W-band (right) WMAP temperature sky maps. Top row shows  $P(g_*|\mathbf{d})$  and bottom three rows show  $P(\hat{\mathbf{n}}|\mathbf{d})$  for three different  $\ell$ -ranges. Note the common preferred axis in both  $\ell = [2, 100]$  and  $[100, 400]$ .

$(l, b) = (110^\circ, 10^\circ)$ .

Further, this same direction is observed in both  $\ell = [2 - 100]$  and  $\ell = [100, 400]$ , indicating that the structure is present over a large range of angular scales. The results are also stable with respect to sky cut, as the same pattern is seen with the KQ75 sky mask as with the KQ85 cut, removing an additional 10% of the sky.

### 5.3. Sensitivity to systematics

Given the nominally strong results found in the previous section, it is imperative to search for possible systematic effects that might explain the observations. In particular, three major sources of uncertainty should be considered in detail, namely non-cosmological foregrounds, correlated noise and asymmetric beams.

First, residual Galactic foregrounds do not a priori ap-

TABLE 1  
SUMMARY OF MARGINAL POSTERIORS FROM WMAP5

| Band  | $\ell$ range | Mask | Amplitude $g_*$        | Direction $(l, b)$      |
|-------|--------------|------|------------------------|-------------------------|
| V     | 2 – 400      | KQ85 | $0.10 \pm 0.04$        | $(130^\circ, 10^\circ)$ |
| V     | 100 – 400    | KQ85 | $0.09[0.084, 0.148]$   | $(130^\circ, 10^\circ)$ |
| V     | 2 – 100      | KQ85 | $-0.07[-0.156, 0.480]$ | $(130^\circ, 15^\circ)$ |
| V     | 2 – 400      | KQ75 | $0.10[-0.100, 0.158]$  | $(130^\circ, 10^\circ)$ |
| V-raw | 2 – 400      | KQ85 | $0.11 \pm 0.036$       | $(130^\circ, 10^\circ)$ |
| V1    | 2 – 400      | KQ85 | $0.12 \pm 0.041$       | $(130^\circ, 10^\circ)$ |
| V2    | 2 – 400      | KQ85 | $0.08 \pm 0.044$       | $(130^\circ, 10^\circ)$ |
| W     | 2 – 400      | KQ85 | $0.15 \pm 0.039$       | $(110^\circ, 10^\circ)$ |
| W     | 100 – 400    | KQ85 | $0.14[-0.097, 0.236]$  | $(110^\circ, 10^\circ)$ |
| W     | 2 – 100      | KQ85 | $0.14[-0.162, 0.470]$  | $(125^\circ, 20^\circ)$ |

NOTE. — In cases with no significant detection, the values for  $g_*$  indicate the maximum posterior value and 95% confidence regions. Otherwise, they indicate posterior mean and standard deviation.

pear as a particularly promising candidate, given that the results are robust with respect to both frequency and sky cut, and the preferred axis does not point towards any natural Galactic direction. Second, in figure 10 we show the posteriors obtained from the raw V-band 5 year sky maps. It should be clear that galactic foregrounds have little impact on these results. Third, extragalactic point sources do also not seem as a likely candidate, because the signature is seen both at low and high  $\ell$ 's, and we never consider multipoles above  $\ell > 400$ , precisely to avoid this type of concerns.

The effect of correlated noise is harder to rule out. On the one hand, returning to the simulated anisotropic CMB realization in Figure 2, we see that the main signature of the ACW model is smoothed structures along the plane normal to the preferred direction, and essentially no modifications along the preferred direction. On the other hand, the main signature of correlated noise is striping along the scan direction.

Next, the ecliptic north pole has Galactic coordinates  $(l, b) = (96^\circ, 30^\circ)$ , which is  $\sim 24^\circ$  ( $32^\circ$ ) away from the preferred direction for W-band (V-band) found in §5.2. The probability of obtaining such a close alignment by chance is  $\sim 10\%$ , ( $\sim 16\%$ ) which is low enough for correlated noise to be considered relevant for this particular case.

To study the magnitude of this effect on  $g_*$ , we analyze realistic V and W-band simulations with correlated noise. These noise simulations were produced and published by the WMAP team in their 1-year data release. To mimic realistic 5-year simulations, we coadd five independent realizations for each differencing assembly. These noise realizations are then added to an isotropic CMB sky realization, and the sum is analyzed using the same procedure as in §5.2. We also analyze two single 1-year W4-band simulations, which serve as a worst-case scenario, as the knee frequency of this band is by far the highest of any WMAP DA, and the overall noise level is higher by a factor of  $\sim 4.5$  than the full 5-year W-band data.

The results from these analyses are shown in Figure 11. The left and middle columns show the simulated 5-year posteriors for V and W-band, respectively, and the right column shows the 1-year W4 posterior. The top row shows  $P(g_*|\mathbf{d})$ , and the bottom panel shows  $P(\hat{\mathbf{n}}|\mathbf{d})$ .

First, note that with realistic 5-year noise no detection is made in either the V- or W-band. Further, the peak sky position is different in the V- and W-bands, and both have a very low significance. It therefore seem unlikely that correlated noise can explain the results found in §5.2.

Still, caution is warranted, as the 1-year W4 posteriors do exhibit traces of anisotropic contributions, with a peak amplitude larger than the observed  $g_*$  in the actual 5-year data. Yet, the match with the structures observed in the real data is less than striking. First, the correlated noise simulations show two independent peaks in the directional posterior, while the WMAP data show one. Second, a detailed study of the joint posteriors for the simulations show that the peak along the ecliptic north pole corresponds to the *negative* peak in  $P(g_*|\mathbf{d})$ , while the WMAP data has a positive  $g_*$  along its preferred direction. Third, the preferred axis found in the WMAP data are further away from the ecliptic pole than the corresponding peak in the simulation posteriors.

Finally, in order to make a complete analysis, we

should also consider the impact of asymmetric beams. Ideally, one would prefer to address this issue in the same manner as correlated noise, by analyzing simulated CMB realizations with asymmetric beams. Unfortunately, we do not have access to such simulations at this time, and it is difficult to do a rigorous analysis. However, there are some arguments against the asymmetric beams hypothesis. First, the effect is observed both at low and high  $\ell$ 's, with very consistent positions. Second, the observed preferred axis is  $\sim 25$ – $30$  degrees away from the ecliptic pole, and the posterior ratio of the ecliptic poles to the maximum posterior is low. Finally, similar signatures are observed in both the V and W bands, and in V1 and V2, which all have slightly different beam patterns.

Nevertheless, at this point it would unwise to make strong claims concerning a possible cosmological interpretation of the signature found in §5.2. Proper analysis of fully realistic 5-year WMAP simulations is required before one can attach cosmological significance to these findings.

## 6. CONCLUSIONS

We have generalized a previously described CMB Gibbs sampler to allow for exact Bayesian analysis of any anisotropic universe models that predicts a sparse signal harmonic space covariance matrix. This generalization involved incorporation of a sparse matrix library into the existing Gibbs sampling code called “Commander”, and implementation of a new sampling algorithm for the anisotropy parameters given a sky map,  $P(\theta|\mathbf{s})$ .

We then considered a special case of anisotropic universe models, namely the Ackerman et al. (2007) model which generalizes the primordial power spectrum  $P(k)$  to include a dependence on direction,  $P(\mathbf{k})$ . Explicit expressions for the resulting covariance matrix is provided in their paper.

We implemented support for this model in our codes, and demonstrated and validated the new tools with appropriate simulations. First, we compared the results from the Gibbs sampler with brute-force likelihood evaluations, and then verified that the input parameters were faithfully reproduced in realistic WMAP simulations.

Finally, we analyzed the five-year WMAP temperature sky maps, and presented for the first time the WMAP posteriors of the ACW model. The results from this analysis are highly intriguing, but we emphasize that the effect of instrumental systematics, particularly in the form of correlated noise, must be better understood before the findings can be given a cosmologically interpretation.

Taken at face value, we find a preferred direction in the W-band WMAP temperature data pointing towards  $(l, b) = (110^\circ, 10^\circ)$  (Galactic longitude and latitude), with an anisotropy amplitude of  $g_* = 0.15 \pm 0.039$ , formally corresponding to a  $3.8\sigma$  detection of  $g_* \neq 0$ . Similar results for  $g_*$  are found for the V-band data, although with a somewhat lower significance ( $g_* = 0.10 \pm 0.04$ ;  $2.5\sigma$ ). The preferred direction is very stable with respect to both data set and multipole range. Figure 12 illustrates the underlying anisotropic contribution for a simulation with parameters corresponding to the W band posterior.

We have not been able to identify a plausible explanation for this effect in terms of known systematics. First, foregrounds do not appear to have much impact

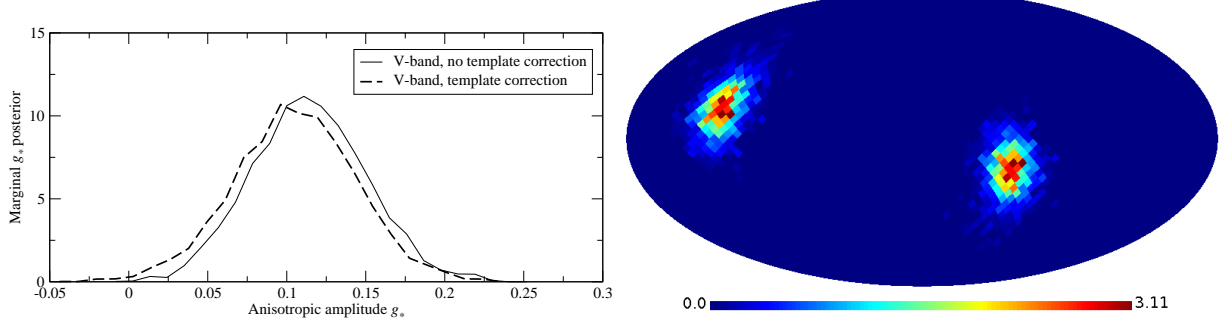


FIG. 10.— Marginal ACW posteriors obtained from the non-template corrected V-band,  $P(\hat{n}|\mathbf{d})$  (right) and  $P(g_*|\mathbf{d})$  (left). Notice how  $P(g_*|\mathbf{d})$  is shifted insignificantly with respect to the template-corrected V-band posterior.

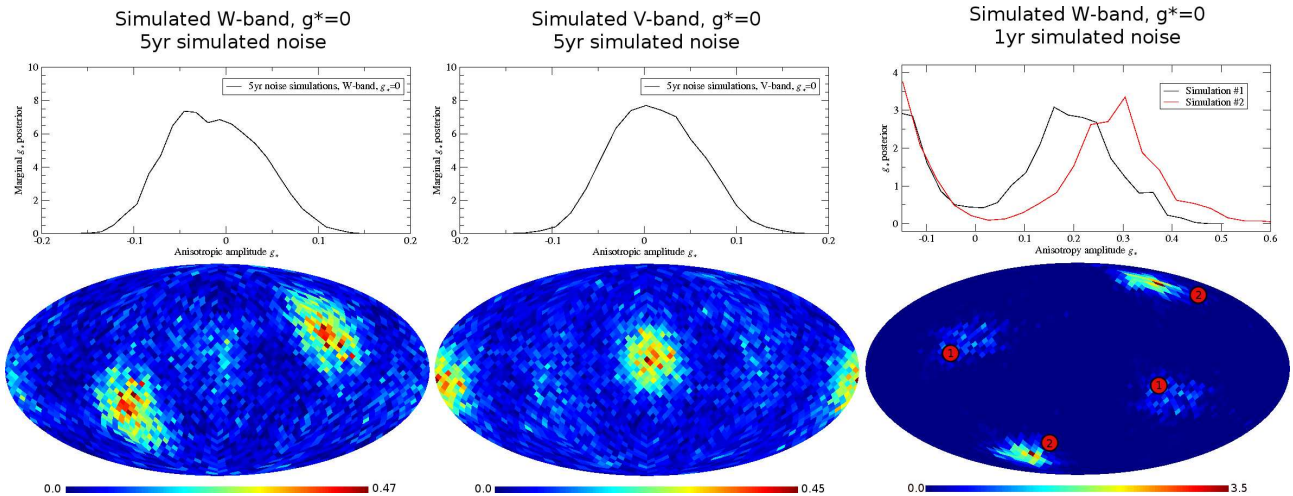


FIG. 11.— Top: Posteriors for  $g_*$  obtained from two 1-year WMAP W4 simulations with correlated noise. Bottom: The preferred direction posterior for one of the two above simulations. The peak positions of the second simulations are indicated by red dots, marked by (1) and (2).

on the results, as consistent results are obtained both from foreground-corrected and raw maps. Second, although correlated noise does lead to a signature similar to the ACW model, its amplitude appears too low in the 5-year data. The least well constrained possibility is that of asymmetric beams, for which we lack proper simulations.

While this particular signature certainly is highly intriguing, we would like to point out that the main purpose of this paper is the demonstration of a general framework for analyzing anisotropic signal models. This is useful both for studying particular universe models (e.g., the ACW model), but also for understanding systematic effects (e.g., correlated noise) in a given data set. We therefore believe that these methods may be useful in a wide range of applications, only some of which have

been demonstrated in this paper.

We thank Ned Wright for extremely useful feedback, and Tim Davis for helping out with the details with his sparse matrix LDL Cholesky decomposition library. We also thank Jeff Jewell, Frode K. Hansen, Magnus Axelson and Kris Górska for useful discussions. We acknowledge use of the HEALPix<sup>5</sup> software (Górska et al. 2005) and analysis package for deriving the results in this paper. We acknowledge the use of the Legacy Archive for Microwave Background Data Analysis (LAMBDA). Support for LAMBDA is provided by the NASA Office of Space Science. The authors acknowledge financial support from the Research Council of Norway.

## REFERENCES

- Ackerman, L., Carroll, S. M., & Wise, M. B. 2007, Phys. Rev. D, 75, 083502
- Armendariz-Picon, C. 2006, Journal of Cosmology and Astroparticle Physics, 3, 2
- Bennett, C. L., et al. 2003, ApJS, 148, 1
- Chu, M., Eriksen, H. K., Knox, L., Górska, K. M., Jewell, J. B., Larson, D. L., O'Dwyer, I. J., & Wandelt, B. D. 2005, Phys. Rev. D, 71, 103002
- Cruz, M., Martínez-González, E., Vielva, P., & Cayón, L. 2005, MNRAS, 356, 29
- Davis, T.A. 2005, ACM Trans. Math. Softw. vol 31 no 4
- de Oliveira-Costa, A., Tegmark, M., Zaldarriaga, M., & Hamilton, A. 2004, Phys. Rev. D, 69, 063516
- Erickcek, A. L., Kamionkowski, M., & Carroll, S. M. 2008, PRL, submitted, [arXiv:0806.0377]
- Eriksen, H. K., Hansen, F. K., Banday, A. J., Górska, K. M., & Lilje, P. B. 2004a, ApJ, 609, 1198
- Eriksen, H. K., et al. 2004b, ApJS, 155, 227
- Eriksen, H. K., et al. 2006, ApJ, 641, 665
- Eriksen, H. K., et al. 2007a, ApJ, 656, 641
- Eriksen, H. K., Huey, G., Banday, A. J., Górska, K. M., Jewell, J. B., O'Dwyer, I. J., & Wandelt, B. D. 2007b, ApJ, 665, L1

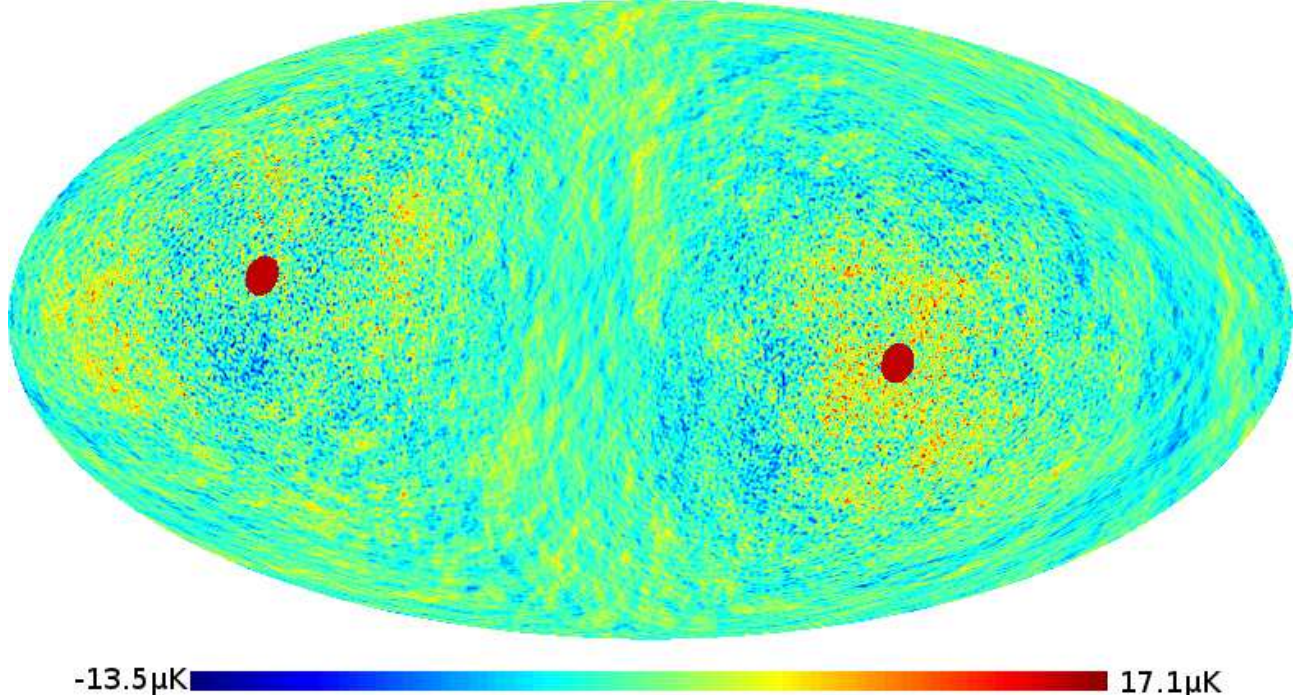


FIG. 12.— A simulated realization drawn from a Gaussian distribution with zero mean and a covariance matrix given by the anisotropic  $\Delta$  term in the ACW model, computed for an asymmetry amplitude of  $g_* = 0.14$  and a preferred direction  $(l, b) = (110^\circ, 10^\circ)$ , marked by red dots. Notice the rotational structure about the preferred direction. The amplitude of the anisotropic component is  $\sim \pm 15\mu\text{K}$ , or  $\sim 3\%$  of the isotropic component.

- Eriksen, H. K., Jewell, J. B., Dickinson, C., Banday, A. J., Górski, K. M., & Lawrence, C. R. 2008a, ApJ, 676, 10  
 Eriksen, H. K., Dickinson, C., Jewell, J. B., Banday, A. J., Górski, K. M., & Lawrence, C. R. 2008b, ApJ, 672, L87  
 Eriksen, H. K., & Wehus, I. K. 2008, ApJS, submitted, [arXiv:0806.3074]  
 Gelman, A., & Rubin, D. 1992, Stat. Sci., 7, 457  
 Gold, B., et al. 2008, ApJS, in press, [arXiv:0803.0715]  
 Górski, K. M., Hivon, E., Banday, A. J., Wandelt, B. D., Hansen, F. K., Reinecke, M., & Bartelmann, M. 2005, ApJ, 622, 759  
 Emir Gümrükçüoglu, A., Contaldi, C. R., & Peloso, M. 2007, Journal of Cosmology and Astro-Particle Physics, 11, 5  
 Gupta, A. K. & Nagar, D. K. 2000, Matrix Variate Distributions  
 Guth, A. H. 1981, Phys. Rev. D, 347  
 Hansen, F. K., Banday, A. J., & Górski, K. M. 2004, MNRAS, 354, 641  
 Hinshaw, G., et al. 2003, ApJS, 148, 63  
 Hinshaw, G., et al. 2007, ApJS, 170, 288  
 Hinshaw, G., et al. 2008, ApJ, submitted, [arXiv:0803.0732]  
 Jaffe, T. R., Banday, A. J., Eriksen, H. K., Górski, K. M., & Hansen, F. K. 2005, ApJ, 629, L1  
 Jarosik, N., et al. 2003, ApJS, 148, 29  
 Jewell, J., Levin, S., & Anderson, C. H. 2004, ApJ, 609  
 Kanno, S., Kimura, M., Soda, J., & Yokoyama, S. 2008, [arXiv:0806.2422]  
 Komatsu, E., et al. 2008, ApJS, in press, [arXiv:0803.0547]  
 Larson, D. L., Eriksen, H. K., Wandelt, B. D., Górski, K. M., Huey, G., Jewell, J. B., & O'Dwyer, I. J. 2007, ApJ, 656, 653  
 Lewis, A., Challinor, A., & Lasenby, A. 2000, ApJ, 538, 473  
 Linde, A. D., 1982, Phys. Lett. B 108, 389  
 Linde, A. D., 1983, Phys. Lett. B 155, 295  
 Linde, A. D., 1994, Phys. Rev. D49, 748  
 Liu, J. S., Monte Carlo Strategies in Scientific Computing, Cambridge, USA: Springer, 2001,  
 Muhkanov, V. F., Chibishev, G. V., & Pis'mah Zh. 1981, Eskp. Teor. Fiz. 33, 549  
 O'Dwyer, I. J., et al. 2004, ApJ, 617, L99  
 Oh, S. P., Spergel, D. N., & Hinshaw, G. 1999, ApJ, 510, 551  
 Pullen, A. R., & Kamionkowski, M. 2007, Phys. Rev. D, 76, 103529  
 Ruhl et al., 2003, ApJ599, 786  
 Runyan et al., 2003, ApJ, J. Suppl. Ser. 149, 265  
 Scott et al., 2003, MNRAS341, 1076  
 Smoot et al., 1992, ApJ396, L1  
 Spergel, D. N., et al. 2007, ApJS, 170, 377  
 Starobinsky, A. A., 1980, Physics Letters B, 91, 99  
 Starobinsky, A. A., 1982, Phys. Lett. B 117, 175  
 Vielva, P., Martínez-González, E., Barreiro, R. B., Sanz, J. L., & Cayón, L. 2004, ApJ, 609, 22  
 Wandelt, Benjamin D. and Larson, David L. and Lakshminarayanan, Arun Phys. Rev. D70,8  
 Yokoyama, S., & Soda, J. 2008, [arXiv:0805.4265]